

Sputter yield of curved surfaces

Herbert M. Urbassek,^{1,*} R. Mark Bradley,² Maureen L. Nietiadi,¹ and Wolfhard Möller³

¹*Physics Department and Research Center OPTIMAS, University Kaiserslautern, Erwin-Schrödinger-Straße, D-67663 Kaiserslautern, Germany*

²*Department of Physics, Colorado State University, Fort Collins, Colorado 80523, USA*

³*Institute of Ion Beam Physics and Materials Research, Helmholtz-Zentrum Dresden-Rossendorf, Bautzner Landstraße 400, 01328 Dresden, Germany*

(Received 21 January 2015; revised manuscript received 28 March 2015; published 20 April 2015)

The mean sputter yield produced by the impact of a single ion depends on the radii of curvature of the target surface at the point of impact. Using the Sigmund model of ion sputtering, we develop analytical formulas for this dependence for the case in which the radii of curvature are large compared to the size of the ion-induced collision cascade; both locally perpendicular and oblique ion impact are considered. The sputter yield is increased for impact on convex surfaces. The influence of surface curvature along the incident-ion azimuth and perpendicular to it are discussed separately. Our analytical results are in good agreement with Monte Carlo simulations for the specific case of 20 keV Ar ion impact on a cylindrical nanowire consisting of amorphous silicon. We also extend the results for this case to small radii of curvature using both Monte Carlo and molecular dynamics simulations.

DOI: [10.1103/PhysRevB.91.165418](https://doi.org/10.1103/PhysRevB.91.165418)

PACS number(s): 79.20.Rf, 79.20.Ap, 61.80.Lj

I. INTRODUCTION

Sputtering of nanoparticles and nanostructured surfaces has recently received increased interest [1]. Applications range from ion irradiation of dust grains in the space environment [2,3] to the sputtering of nanoparticles supported on flat surfaces [4].

Most previous studies focus on the irradiation of spherical particles. Molecular dynamics simulations have been employed to analyze specific cases [5–10]. A recent study [11,12] systematically explores the size dependence of the sputtering of a sphere by a single ion and finds that for large radii R and perpendicular impact, the sphere's sputter yield, Y_R^{sphere} , is greater than that of a flat surface, Y_∞ :

$$Y_R^{\text{sphere}} = Y_\infty \left[1 + \left(\frac{\beta}{\alpha} \right)^2 \frac{a}{R} \right]. \quad (1)$$

Here a is the mean depth at which the ion-induced collision cascade deposits its energy below the surface of a flat target, and α and β denote the longitudinal and lateral widths of the energy deposition profile. In that study deviations from Eq. (1) for small sphere radii are also investigated by Monte Carlo (MC) and molecular dynamics (MD) simulations for the specific case of 20 keV Ar ions impinging on amorphous silicon (a-Si) spheres [12].

The effect of local surface curvature on the sputtering of nonspherical particles has not been explored nearly as well. In their review [1] Krasheninnikov and Nordlund give an overview of recent research on ion irradiation of nanostructured and two-dimensional systems which concentrates on carbon systems such as nanotubes and graphene layers in particular. Ronning *et al.* [13] review available experimental work on irradiation of semiconducting nanowires that focuses on ion implantation. Prototype electronic, photonic, and sensing devices based on semiconducting nanowires have been developed [13]. More recently Ronning and coworkers

extended their work to the sputtering of GaAs and ZnO nanowires and demonstrated that the sputter yields attain a maximum if the ion range matches the nanowire diameter [14,15]. Finally, Greaves *et al.* [16] showed that the sputter yield of a cylindrical Au nanorod that is subjected to 80 keV Xe irradiation can exceed the yield of a flat surface by more than an order of magnitude. These examples show that sputtering of nanorods and nanowires is currently being vigorously explored; however, a general assessment of how curved nano-objects sputter has been lacking.

In the present paper we explore how the sputter yield produced by the impact of a single ion on an arbitrarily curved surface deviates from that of a flat surface. Using the Sigmund model of ion sputtering [17], analytical results are obtained in Sec. II for surfaces whose radii of curvature are large compared to the depth of the energy deposition profile, a . Our results show that the sputter yield depends on the geometrical form of the surface only via the curvature radius R_1 in the direction of the ion impact azimuth and via the curvature radius R_2 perpendicular to it. We also establish that to find the yield for an arbitrarily curved surface, it is sufficient to study impacts on cylinders of radius R for the special cases in which $R_1 = R$ and $R_2 = \infty$ (impacts normal to the cylinder axis) and in which $R_1 = \infty$ and $R_2 = R$ (central impacts).

In order to test these results and to extend them to smaller surface curvatures, we perform MC simulations for the special case of 20 keV Ar impact on a-Si nanocylinders. We simulate impacts normal to the cylinder axis and central impacts for a range of cylinder radii R ; these results will be presented in Sec. IV B. Our MC results validate the analytical theory for large radii of curvature. In addition they allow us to extend our results to smaller curvature radii. Finally we perform MD simulations to corroborate our findings for the case of small cylinder radii.

II. ANALYTICAL THEORY

Consider the impact of a single ion with energy ϵ at a point on the surface of an elemental material. The local angle of

*urbassek@rhrk.uni-kl.de; <http://www.physik.uni-kl.de/urbassek/>

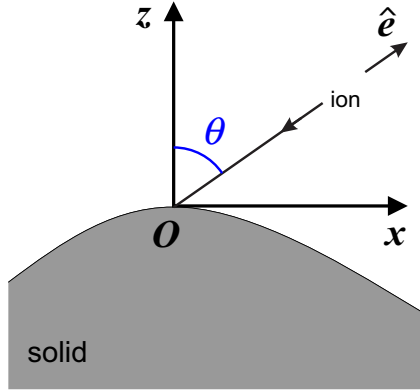


FIG. 1. (Color online) Impact of a single ion at the point O on the solid surface. The z axis is normal to the surface at O and the ion's direction of incidence $-\hat{e}$ is in the x - z plane. The local angle of incidence is θ .

incidence of the ion will be denoted by θ . We place the origin O at the point of impact and put the z axis along the outward-pointing normal to the surface, as shown in Fig. 1. We orient the x and y axes so that the ion's direction of incidence $-\hat{e}$ lies in the x - z plane and is given by $-\hat{e} = -\hat{x} \sin \theta - \hat{z} \cos \theta$. Let $h = h(x, y)$ be the height of the surface above the point (x, y) in the x - y plane. (In the figure, $h \leq 0$.)

Our goal is to compute the average number of sputtered atoms Y using the Sigmund model of ion sputtering. The value of Y depends upon θ and the shape of the surface near the point of impact.

We will assume that the principal radii of curvature of the surface at O are much larger than the mean depth of energy deposition a . Sputtering is appreciable only at surface points whose distance to O is of order a . For these points, we may approximate h by discarding terms of third order and higher terms from its Taylor series: we set

$$h(x, y) = \frac{1}{2} K_{11} x^2 + K_{12} xy + \frac{1}{2} K_{22} y^2, \quad (2)$$

where

$$K_{ij} \equiv \frac{\partial^2 h}{\partial x_i \partial x_j}(0, 0) \quad (3)$$

for $x_1 = x, x_2 = y$.

Recently the so-called crater function formalism has been introduced as a tool to calculate the effects of ion irradiation on surfaces [18,19]. While there are inconsistencies in the original approach [20,21], Harrison and Bradley [21] pointed out that these difficulties can be surmounted by properly including the curvature dependence of the crater function in the theory.

In the crater function formalism of Harrison and Bradley, the crater function $F(x, y, \theta, K_{11}, K_{12}, K_{22})$ is defined to be minus the average change in the surface height h above the point (x, y) in the x - y plane that occurs as a result of the ion impact [21]. The zeroth-order moment of the crater function is

$$\begin{aligned} M &= M(\theta, K_{11}, K_{12}, K_{22}) \\ &= \int_{-\infty}^{\infty} \int_{-\infty}^{\infty} F(x, y, \theta, K_{11}, K_{12}, K_{22}) dx dy. \end{aligned} \quad (4)$$

The average sputter yield is given by

$$Y = M(\theta, K_{11}, K_{12}, K_{22}) / \Omega, \quad (5)$$

where Ω is the atomic volume. For convenience, we set

$$M_{K_{11}} = M(\theta, K_{11}, 0, 0), \quad (6)$$

$$M_{K_{12}} = M(\theta, 0, K_{12}, 0), \quad (7)$$

and

$$M_{K_{22}} = M(\theta, 0, 0, K_{22}). \quad (8)$$

By assumption, the K_{ij} 's are small compared to $1/a$. We may therefore expand M in powers of the K_{ij} 's and only retain terms up to first order. This yields

$$\begin{aligned} M(\theta, K_{11}, K_{12}, K_{22}) &\cong M(\theta, 0, 0, 0) + \left. \frac{\partial M_{K_{11}}}{\partial K_{11}} \right|_{K_{11}=0} K_{11} \\ &\quad + \left. \frac{\partial M_{K_{12}}}{\partial K_{12}} \right|_{K_{12}=0} K_{12} + \left. \frac{\partial M_{K_{22}}}{\partial K_{22}} \right|_{K_{22}=0} K_{22}. \end{aligned} \quad (9)$$

$M(\theta, 0, 0, 0)$ and the partial derivatives of the $M_{K_{ij}}$'s that appear on the right-hand side of Eq. (9) were evaluated in Ref. [21]. Inserting these results into Eq. (9) and using Eq. (5), we obtain

$$Y = Y_{\infty} (1 - ag_1 K_{11} - ag_2 K_{22}). \quad (10)$$

The sputter-yield correction functions g_1 and g_2 are given by

$$g_1(\theta) = \frac{A^2 B_2}{2B_1^2} + \frac{A^3 C}{B_1^3} + \frac{B_2}{2B_1} + \frac{3AC}{B_1^2}, \quad (11)$$

$$g_2(\theta) = \frac{1}{\alpha^2} \left(\frac{B_2}{2} + \frac{AC}{B_1} \right), \quad (12)$$

where α and β denote the longitudinal and lateral widths of the energy deposition profile and

$$a_{\alpha} = a/\alpha,$$

$$a_{\beta} = a/\beta,$$

$$A = a_{\alpha}^2 \sin \theta,$$

$$B_1 = a_{\alpha}^2 \sin^2 \theta + a_{\beta}^2 \cos^2 \theta,$$

$$B_2 = a_{\alpha}^2 \cos \theta,$$

$$C = \frac{1}{2} (a_{\beta}^2 - a_{\alpha}^2) \sin \theta \cos \theta.$$

The functions $g_1(\theta)$ and $g_2(\theta)$ are positive for all angles of incidence $\theta < 90^\circ$.

In the Sigmund model, the mean distance that a surface point recedes as a result of an ion impact is proportional to the energy density that is deposited there by the collision cascade [17]. We will denote the constant of proportionality by Λ . The sputter yield for a flat surface is then

$$Y_{\infty} = \frac{a^2 \epsilon \Lambda}{(2\pi)^{1/2} a \alpha \beta \sqrt{B_1}} \exp \left(\frac{A^2}{2B_1} - \frac{a_{\alpha}^2}{2} \right). \quad (13)$$

For a flat surface, $K_{11} = K_{22} = 0$ and Y reduces to Y_{∞} , as it must. A sphere of radius R has $K_{11} = K_{22} = -1/R$. In the

case of normal-incidence ion impact,

$$g_1(0) = g_2(0) = \frac{1}{2} \left(\frac{\beta}{\alpha} \right)^2, \quad (14)$$

and we recover Eq. (1) for the mean sputter yield of the sphere at perpendicular impact. We also immediately obtain the generalization of this result to arbitrary impact angles θ :

$$Y_R^{\text{sphere}}(\theta) = Y_\infty \left\{ 1 + [g_1(\theta) + g_2(\theta)] \frac{a}{R} \right\}. \quad (15)$$

The sputter yield of a general surface for perpendicular incidence is given by

$$Y = Y_\infty \left[1 - a \left(\frac{\beta}{\alpha} \right)^2 H \right], \quad (16)$$

where $H = (K_{11} + K_{22})/2$ is the mean curvature of the surface [22]. Thus, the sputter-yield correction to the flat-surface yield is positive for a concave surface and is negative for a convex surface.

Sputtering of a cylinder

For later use, we will apply our results to the sputtering of a solid cylinder of radius R . The impact of the ion on the cylinder's surface is characterized by two angles (see Fig. 2): ϕ characterizes the tilt towards the cylinder axis, while ϑ characterizes the impact parameter of the ion relative to the cylinder's axis.

We are interested in the cases of incidence normal to the cylinder axis ($\phi = 0$) and of central impacts on the cylinder ($\vartheta = 0$). For normal-to-axis impacts, $\theta = \vartheta$, $K_{11} = -1/R$, $K_{22} = 0$, and hence

$$Y = Y_\infty \left[1 + g_1(\vartheta) \frac{a}{R} \right]. \quad (17)$$

For central impacts, on the other hand, $\theta = \phi$, $K_{11} = 0$, $K_{22} = -1/R$, and

$$Y = Y_\infty \left[1 + g_2(\phi) \frac{a}{R} \right]. \quad (18)$$

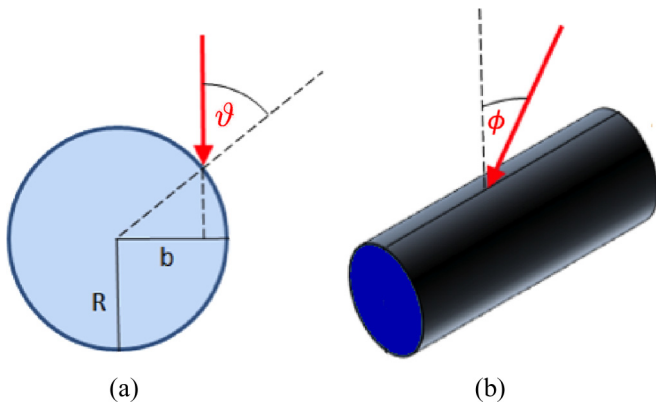


FIG. 2. (Color online) Sketch of the definition of impact angles on a cylindrical surface. (a) Normal-to-axis impacts are characterized by the incidence angle ϑ and the impact parameter b . (b) Central impacts are characterized by the incidence angle ϕ .

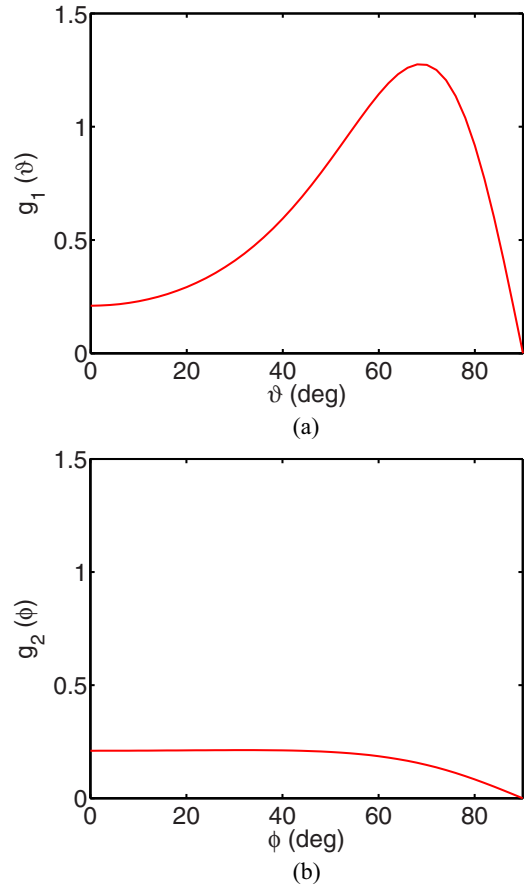


FIG. 3. (Color online) Sputter-yield correction functions (a) $g_1(\vartheta)$ for normal-to-axis impacts and (b) $g_2(\phi)$ for central impacts, as obtained by analytical theory for a cylinder surface, Eqs. (11) and (12).

Here the g_i 's are the sputter-yield correction functions (11) and (12) evaluated for the angles indicated.

In Fig. 3, we plot these two functions. We adopt the parameters $a_\alpha = 1.70$ and $a_\beta = 2.62$ that are appropriate for 20 keV Ar impact on a-Si (see Sec. IV below and Ref. [12]). Both curvature corrections are positive for all angles, since, in the case of the Sigmund model, the collision cascade deposits more energy on the cylinder's surface than on a flat surface. At perpendicular incidence, the sputter-yield correction function is 0.21. At glancing incidence, it vanishes; note that in this case the flat-surface sputter yield also vanishes, since the ion is not able to deposit energy in the surface.

At oblique incidence, the central-impact correction, g_2 , shows only a weak dependence on the angle ϕ up to about 60° , and then monotonically decreases. For normal-to-axis impacts, however, the correction increases with incidence angle and goes through a maximum at $\vartheta = 69^\circ$, where g_1 assumes a value roughly 6 times larger than at perpendicular incidence. At such angles, the impact parameter b is already $0.93R$ and the center of the collision cascade is close to the cylinder periphery; the high-energy deposition at the curved surface maximizes sputtering.

Equations (17) and (18) show that to test the Sigmund theory's predicted forms for $g_1(\theta)$ and $g_2(\theta)$ using MC

simulations, it is sufficient to simulate normal-to-axis and central impacts on a cylinder. We therefore will carry out simulations of ion impacts on cylinders for these two special cases.

III. SIMULATION METHODS

We study the sputtering of cylinders by 20 keV Ar ions using both MC and MD simulations. The techniques employed are analogous to those used in a previous study of the sputtering of nanospheres [12]. We assemble the essential details for the convenience of the reader.

The MC code TRI3DST employed in this paper makes use of collisional algorithms which are taken from the sputtering version of TRIM.SP [23] of the popular simulation code TRIM [24,25], with several modifications as described in a recent paper on 3D dynamic simulations [26]. Basically, the propagation of incident projectiles and the generated recoils in an amorphous medium are traced as a sequence of binary collisions in a repulsive screened Coulomb potential with the Kr-C parametrization [27]. Electronic stopping is included as an equipartition of nonlocal (according to Lindhard and Scharff [28]) and local (according to Oen and Robinson [29]) energy losses. TRI3DST is applicable to homogeneous three-dimensional multicomponent bodies with surfaces that can be described by an analytical function. For the transmission of sputtered atoms through the surface, a locally planar surface barrier is assumed with the local surface normal being deduced from the analytical contour function. This means that any dependence of the surface binding energy on the local curvature is not taken into account. The surface binding energy is set to $U = 4.7$ eV in accordance with the enthalpy of sublimation of Si. Data are based on 10^5 impacts for each combination of cylinder radius and impact angle.

MD simulations are performed for small cylinder radii, $R = 1, 1.5, 2.5,$ and 3.5 nm, and only for perpendicular impact ($\vartheta = 0, \phi = 0$). Cylinders are cut out of an a-Si target that was prepared according to the recipe of Luedtke and Landman [30], and then relaxed for 50 ps. The cylinders have a length of 10 nm; periodic boundary conditions are employed along the axial direction to emulate an infinitely long cylinder. Silicon atoms interact via the Stillinger-Weber potential [31]. For small interaction distances the potential is fitted to the Ziegler-Biersack-Littmark (ZBL) potential [32]. Ar and Si atoms interact via the ZBL potential. For each cylinder radius, 1000 impacts have been simulated for a time of 3 ps. The impacts differed in that in each case a different impact point was chosen at random on the cylinder surface. All atoms that are a distance greater than 7.54 \AA from the original cylinder surface (i.e., twice the cutoff radius of the Stillinger-Weber potential) are considered to have been sputtered.

IV. SIMULATION RESULTS

In this section we present simulation results for 20 keV Ar impacts on a-Si cylinders. We first present and discuss the information obtained from the MC calculations; the comparison with MD data is given in Sec. IV D.

From previous simulations [12], we know the sputter yield of a flat target, $Y_\infty(\theta)$, as a function of the incidence angle.

In addition, the geometrical parameters describing the spatial distribution of the energy deposited in a flat target are known: they are $a = 208.9 \text{ \AA}$, $\alpha = 123.0 \text{ \AA}$, and $\beta = 79.7 \text{ \AA}$.

A. Perpendicular impact

We first study sputtering for perpendicular impacts, i.e., for $\vartheta = 0$ and $\phi = 0$. Figure 4(a) compares the MC results to the prediction of the analytical theory,

$$Y = Y_\infty \left[1 + \frac{1}{2} \left(\frac{\beta}{\alpha} \right)^2 \frac{a}{R} \right] = Y_\infty \left(1 + 0.21 \frac{a}{R} \right), \quad (19)$$

where the last equality holds for our values for α and β . We observe good agreement for $R \gtrsim 2a$. We also include the MC results obtained for spheres of radius R in Ref. [12]; the analytical prediction for the curvature correction for the sphere [see Eq. (1)] is exactly twice that for the cylinder. The MC data corroborate this prediction nicely.

For cylinders with smaller radii [see Fig. 4(b)], we find that the sputter yield goes through a maximum at $R/a \cong 0.5$; here the yields are a factor of around 6.3 higher than for the flat target. This increase is due to the fact that with decreasing R the

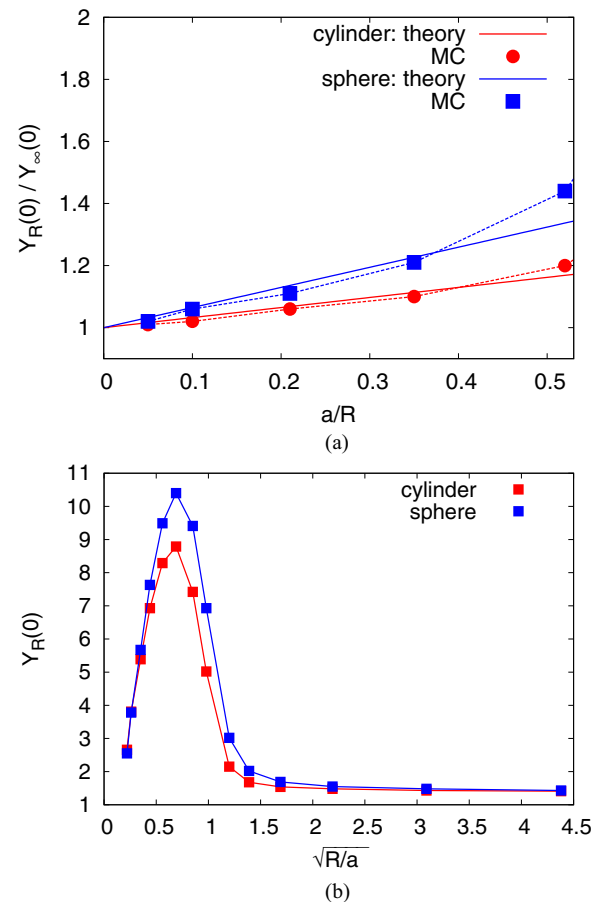


FIG. 4. (Color online) Sputter yield of a cylinder for perpendicular impact $Y_R(\vartheta = 0, \phi = 0)$, normalized to the sputter yield of a flat surface, Y_∞ . (a) MC data for cylinders with large radii compared to the theoretical result Eq. (19). (b) MC data for all cylinders, compared to the data for spheres. Data plotted vs $\sqrt{R/a}$ in order to compress the abscissa axis.

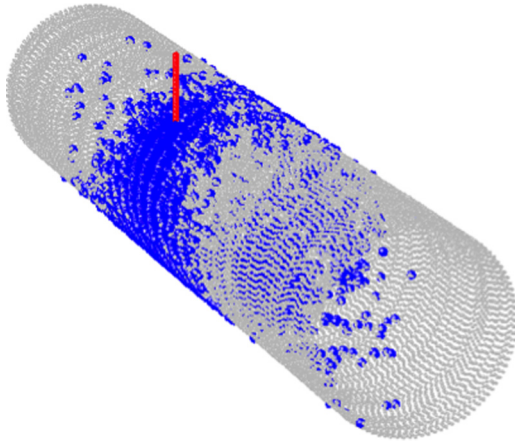


FIG. 5. (Color online) Emission-site distribution for impact on a cylinder of radius $R/a = 0.19$ with impact parameter $b = 0.6R$ and $\phi = 0$. Direction of ion incidence and impact point are indicated by the red line. The distribution has been obtained with 1000 incident projectiles.

cylinder surface moves closer to the center of the distribution of deposited energy; the energy density at the cylinder surface increases and hence the sputter yield does as well. For even smaller radii, the sputter yield decreases again, since less and less energy is deposited within the cylinder. A sputter yield maximum was also found by Johannes *et al.* in a Monte Carlo study of the sputtering of nanowires [14].

For small radii ($R \ll a$), the sputter yields of spheres and cylinders of the same radius nearly coincide. At these small radii, the deposited-energy density in the irradiated particle is quite homogeneous and so the sputter yield is determined mainly by the active surface area from which atoms are sputtered. At first glance, one would expect a long cylinder to have a larger sputter yield than a sphere of equal radius due to its larger surface area. However, the lateral width of the collision cascade is also influenced by the small radius; fewer recoils reach lateral distances greater than R than for a flat target, effectively limiting the lateral width of the deposited-energy distribution to a value of order R . As a consequence, the effective surface area from which a cylinder with a small value of R sputters is similar to that of a sphere of equal radius, and hence the sputter yields of these two objects become comparable for $R \ll a$. This fact is illustrated by plotting the sites where atoms are sputtered from a narrow cylinder (see Fig. 5). This figure demonstrates that the surface region where sputtering from narrow cylinders occurs is limited in the axial direction. This figure shows the emission site distribution of atoms sputtered from a cylinder with the rather small radius $R = 0.19a$. We observe that indeed the axial width of the emission sites (which is a measure of the distribution of the deposited energy at the cylinder's surface) is comparable to the cylinder's radius.

B. Oblique incidence

We study sputtering by obliquely incident ions first for normal-to-axis impacts ($\phi = 0$) with a range of ϑ values, and then for central impacts ($\vartheta = 0$) with a range of ϕ values.

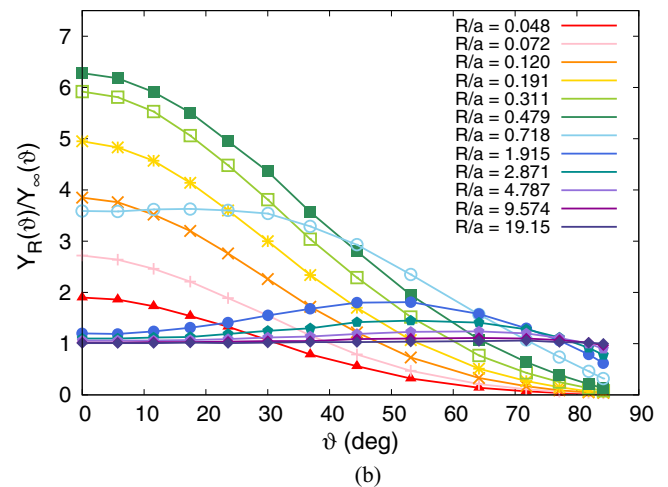
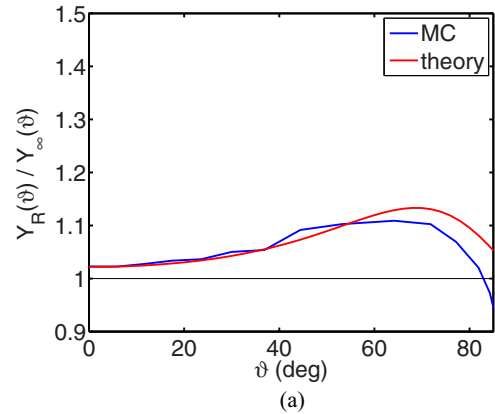


FIG. 6. (Color online) (a) Ratio of the sputter yield of a cylinder of radius R , Y_R , to the sputter yield of a flat target, Y_∞ , as a function of the impact angle ϑ for normal-to-axis impacts, i.e., for $\phi = 0$. (a) MC data for a cylinder of radius $R = 9.574a$ compared to the analytical result given by Eq. (17). (b) All MC data.

The angular dependence of the sputter yield for cylinders of various radii R is displayed in Fig. 6; the data are divided by the sputter yields of a flat target of the same incidence angle in order to highlight the changes brought about by the cylinder's curvature. For a large cylinder radius ($R = 9.574a$), the MC results are compared to the analytical prediction given by Eq. (17) in Fig. 6(a). The form of the sputter-yield correction has already been discussed in Sec. II A. We observe very satisfactory agreement up to angles of around 70° . At higher angles, the theoretical result remains qualitatively correct in predicting a drop-off of the sputter-yield correction, but the MC data show a slightly stronger effect.

Figure 6(b) shows how the angular dependence of $Y_R(\vartheta)/Y_\infty(\vartheta)$ changes if the cylinder's radius is varied. In order to discuss the complex behavior observed, we note that the sputtering behavior of nanoparticles shows distinct differences from that of a flat surface. A flat surface shows only *backward sputtering*, while sufficiently small nanoparticles will also feature *forward sputtering*. In addition, *lateral sputtering* may occur if an ion impinges at near grazing incidence. Emission in the forward and lateral directions is illustrated in the emission site distribution, Fig. 5.

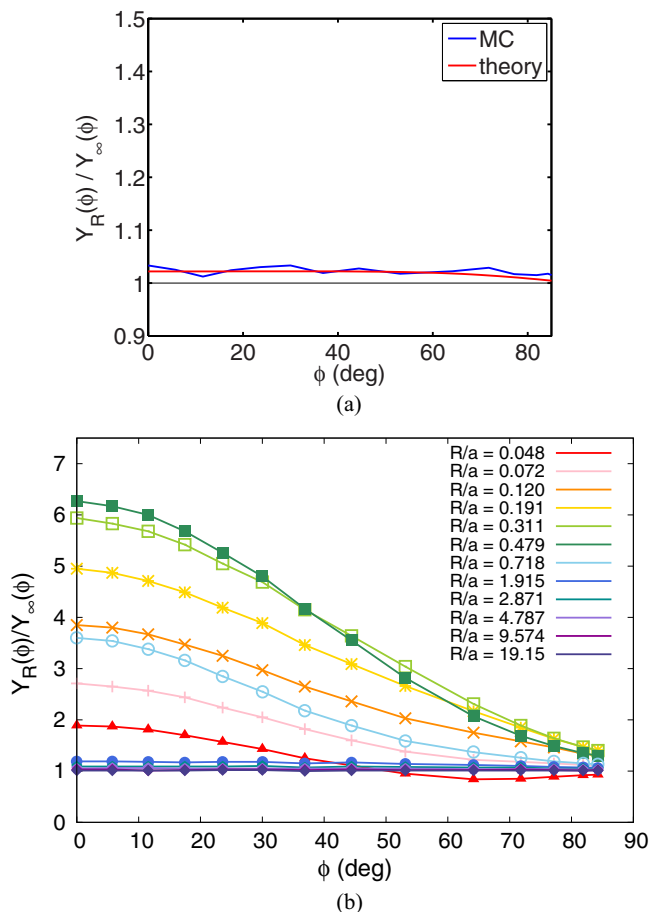


FIG. 7. (Color online) (a) Ratio of the sputter yield of a cylinder of radius R , Y_R , to the sputter yield of a flat target, Y_∞ , as a function of the impact angle ϕ for central impacts, i.e., for $\vartheta = 0$. (a) MC data for a cylinder of radius $R = 9.574a$ compared to the analytical result given by Eq. (18). (b) All MC data.

We identify the following general trends in the sputtering behavior of cylinders [see Fig. 6(b)]:

(1) For large radii ($R \geq 2a$), sputtering is enhanced at intermediate angles of incidence; the reason is that for these impact angles lateral sputtering at the cylinder periphery gives an additional contribution to the sputter yield.

(2) At near glancing incidence angles the yield decreases below that of the infinite medium; this is plausible since a near glancing incidence ion has a shorter trajectory under the curved surface than it would in a flat target.

(3) For smaller radii ($R \sim a$) we see a general enhancement of sputtering for all impact angles $0 < \vartheta < 40^\circ$. At these angles, the center of the collision cascade is situated close to the cylinder axis, and a large range of incidence angles is favorable for sputtering.

(4) For even smaller radii ($R/a \lesssim 0.5$) forward sputtering becomes dominant.

Figure 7 displays the analogous data for central impacts. In this case $\vartheta = 0$ and the angle ϕ is varied. For a large cylinder radius ($R = 9.574a$) our analytical result, Eq. (18), is well corroborated by the MC data throughout the entire range of ϕ values. The angular dependence of the sputter yield for smaller radii [see Fig. 7(b)] is simpler than the ϑ dependence discussed

above. The data primarily show a general increase of sputtering above the values for a flat target as soon as the cylinder radius is $\lesssim a$; this feature is analogous to item 3 discussed above and is caused by forward sputtering for thin cylinders. For oblique incidence angles, the deviations from the flat-target sputter yields become less pronounced, since for central impacts (i.e., for $\vartheta = 0$) the cylinder's curvature along the ion incidence azimuth vanishes and the ion sees a target extending far along this direction. As a consequence the sputter yield does not fall below its value for a flat surface at glancing incidence angles; this is in contrast to item 2 above. The slight dip seen for the smallest cylinder radius ($R = 0.048a$) at incidence angles around $\phi = 60^\circ$ – 70° is caused by the increased probability that ions fully penetrate the thin cylinder and deposit less energy than in a flat target.

C. Average sputter yield

The average sputter yield of a cylinder, $\langle Y_R \rangle$, can be defined as follows. Consider a unidirectional flux Φ of projectile ions incident on a cylinder segment of length ℓ ; it sputters a number of $2R\ell\Phi\langle Y_R \rangle$ atoms from the cylinder per unit time. Using the impact parameter $b = x/R = \sin \vartheta$ (see Fig. 2), we can write

$$\langle Y_R \rangle = \frac{1}{R} \int_0^R Y_R(b) db. \quad (20)$$

$\langle Y_R \rangle$ depends on the angle $90^\circ - \phi$ the incident ions make with the the cylinder axis; here we calculate the yield for normal-to-axis impacts, i.e., for $\phi = 0$. The results shown in Fig. 8 demonstrate that with increasing curvature the average yield rises and reaches a maximum at $R/a = 0.479$, where the average yield is increased by a factor of 2.70. This behavior is comparable to the results for sputtering of a sphere [12], where the maximum occurs at $R/a = 0.957$ with a maximum increase of 2.24. For small radii the yield decreases once more, since less energy is deposited in the cylinder and accordingly less is available for sputtering.

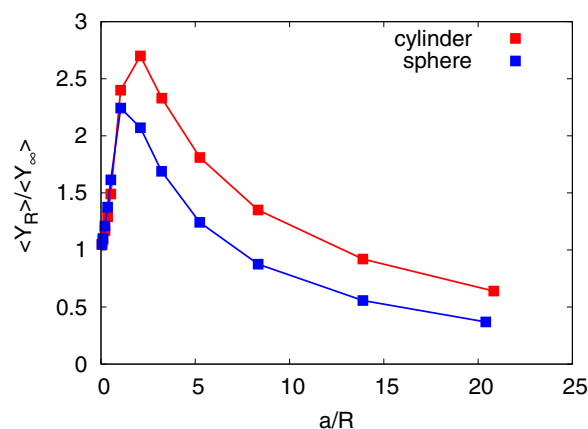


FIG. 8. (Color online) Average sputter yield, $\langle Y_R \rangle$, of a cylinder of radius R for central impact (i.e., for $\phi = 0$) as a function of the dimensionless inverse cylinder radius, a/R . Data have been normalized to the value for a flat target. Data for impacts on a sphere of radius R (Ref. [12]) have been added for comparison.

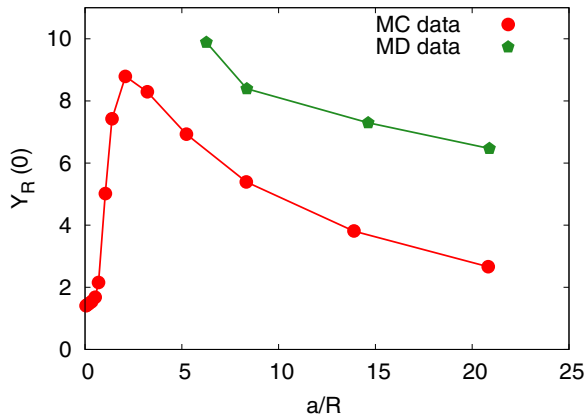


FIG. 9. (Color online) Absolute sputter yields for central impact ($\vartheta = \phi = 0$) as a function of the dimensionless inverse cylinder radius, a/R . The MC data are compared to the results of MD simulations.

D. MD results for small cylinders

For the narrowest cylinders studied, the range of validity of the MC model may have been exceeded, since several effects not included in this model may play a role. First, the surface binding energy of atoms may be reduced at strongly curved surfaces; next, the nanorod may be totally fragmented by the impacting ion; and finally collision spikes [33–35] may lead to abundant sputtering. All these effects are included naturally

in MD simulations and hence we will compare our MC results for the case of small cylinder radii to the results from MD simulations.

Figure 9 compares the results of MD simulations for cylinders of radius $R = 1\text{--}3.5$ nm with the MC data; only collisions with perpendicular impact (i.e., $\vartheta = \phi = 0$) were simulated. We observe that the MD results are consistently larger than the MC data. This finding is similar to our previous result for spheres [12], and the discussion proceeds analogously. There are subtle differences between the MC and MD algorithms which, however, only have a minor effect on the results: (i) The differences in the surface binding energies in MD and MC (which are around 8%) lead to differences in the sputter yield of the same relative size. (ii) The influence of electronic stopping, which is included in the MC but not in the MD simulations, leads to further sputter-yield differences of around 10%. (iii) Different screened Coulomb potential parametrizations have been chosen in the MC and MD simulations (Kr-C and ZBL, respectively). However, in selected MC simulations using the ZBL screening function, the influence on the results was shown to be negligible.

These effects cannot explain the difference between the MC and MD sputter yields for small cylinder radii in Fig. 9, which amount to a factor of almost 2. We attribute these differences to the action of collision spikes which are included in a natural way in MD, but not in MC simulations. In order to demonstrate the effect of the spikes, a number of snapshots of the sputtered cylinders at 3 ps after ion impact are displayed

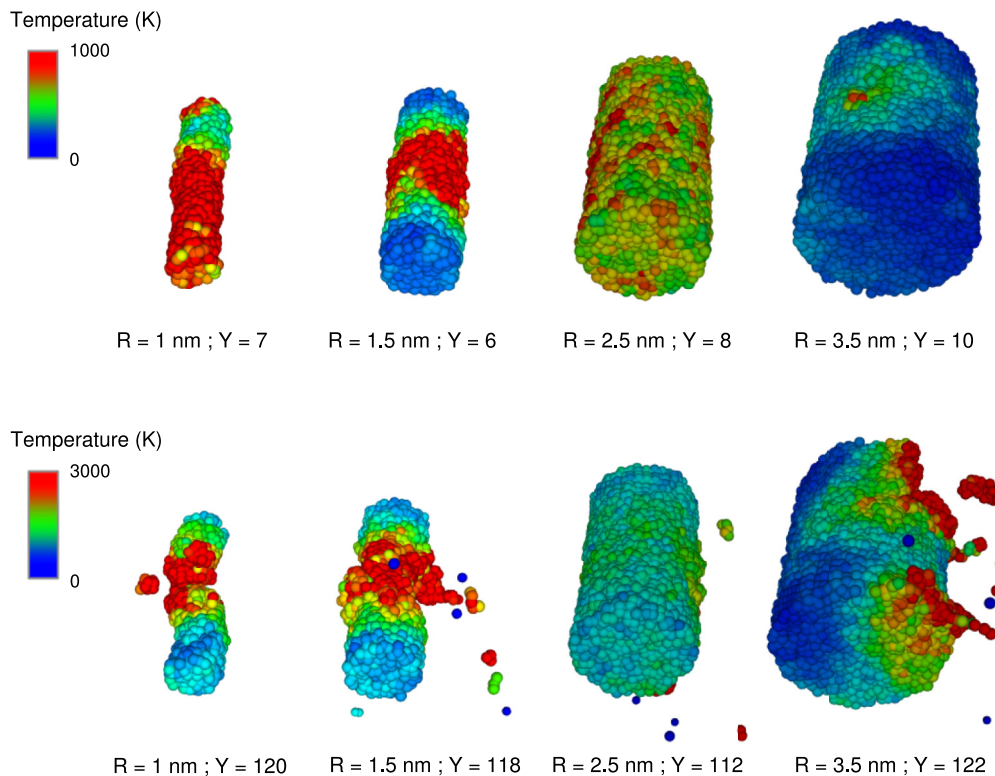


FIG. 10. (Color online) Perspective view of sputtered cylinders 3 ps after ion impact in MD simulations. In all cases, the ion was incident from the top ($\vartheta = \phi = 0$) onto the middle of the cylinder segments displayed. Atoms are colored according to the local temperature. (a) Representative events in which impact leads to the average sputter yield. (b) Events with abundant sputtering. Note the change in color code between (a) and (b).

in Fig. 10. The top row shows representative events in which the average number of atoms is sputtered; the bottom row shows particularly abundant sputtering events. For the smallest cylinder radii ($R \leq 1.5$ nm), the cylinder starts melting close to the irradiated zone even for an average energy deposition. For events that produce abundant sputtering, on the other hand, the cylinder is nearly torn in two by the impact. For larger radii, e.g., for $R = 3.5$ nm, chunks of matter are violently ejected from the cylinder's surface. In summary, these snapshots demonstrate that collision spikes increase the sputter yield above the values predicted by MC simulations.

V. SUMMARY

In this paper, the mean sputter yield produced by the impact of a single ion on a curved solid surface was studied analytically and using Monte Carlo and molecular dynamics simulations. Using the Sigmund model of ion sputtering, analytical formulas were developed for the sputter yield of an arbitrarily curved surface for the case that the radii of curvature at the point of ion impact are large compared to the mean depth at which the ion deposits its energy, a . We tested the validity of these formulas for the specific case of a cylindrical target by comparing to a set of Monte Carlo simulations of the irradiation of an amorphous Si cylinder by 20 keV Ar ions. We found good agreement for large cylinder radii R . For smaller cylinder radii, the sputter yield goes through a maximum and decreases again when R is reduced below a . Our molecular dynamics simulations revealed that collision

spikes that produce copious ejecta become important in this regime.

In detail our study reveals the following features:

(1) For large radii of curvature and angles of incidence that are not too close to grazing, sputter yields from convex surfaces are greater than for a flat surface, and less for concave surfaces.

(2) For perpendicular incidence a simple expression, Eq. (16), allows one to easily assess the sputter-yield correction.

(3) For small radii of curvature, we discussed the effect of curvature along the ion incidence azimuth and perpendicular to it separately by studying impacts on cylindrical surfaces.

Curvature along the ion incidence azimuth leads to

(a) enhanced sputtering at intermediate angles of incidence due to lateral sputtering from the cylinder;

(b) reduced sputtering for impacts at glancing angles; and

(c) a strong contribution to emission from forward sputtering for cylinder radii $R \lesssim 0.5a$.

(4) Curvature perpendicular to the ion incidence azimuth increases sputtering if the cylinder radius becomes smaller than a , and forward sputtering becomes possible.

ACKNOWLEDGMENTS

M.L.N. is grateful for support by the *Deutsche Forschungsgemeinschaft* via the Research Unit 845 *Self-organized nanostructures induced by low-energy ion beam erosion*. R.M.B. would like to thank the National Science Foundation for its support through Grant No. DMR-1305449.

-
- [1] A. V. Krasheninnikov and K. Nordlund, *J. Appl. Phys.* **107**, 071301 (2010).
- [2] T. A. Cassidy and R. E. Johnson, *Icarus* **176**, 499 (2005).
- [3] E. M. Bringa, S. O. Kucheyev, M. J. Loeffler, R. A. Baragiola, A. G. G. M. Tielens, Z. R. Dai, G. Graham, S. Bajt, J. P. Bradley, C. A. Dukes *et al.*, *Astrophys. J.* **662**, 372 (2007).
- [4] A. Klimmer, P. Ziemann, J. Biskupek, U. Kaiser, and M. Flesch, *Phys. Rev. B* **79**, 155427 (2009).
- [5] R. Kissel and H. M. Urbassek, *Nucl. Instrum. Methods Phys. Res., Sect. B* **180**, 293 (2001).
- [6] R. Kissel and H. M. Urbassek, *Int. J. Mass Spectrom.* **208**, 29 (2001).
- [7] S. Zimmermann and H. M. Urbassek, *Int. J. Mass Spectrom.* **272**, 91 (2008).
- [8] T. T. Järvi, J. A. Pakarinen, A. Kuronen, and K. Nordlund, *Europhys. Lett.* **82**, 26002 (2008).
- [9] T. T. Järvi and K. Nordlund, *Nucl. Instrum. Methods Phys. Res., Sect. B* **272**, 66 (2012).
- [10] J. C. Jimenez-Sanz, A. M. C. Perez-Martin, and J. J. Jimenez-Rodriguez, *Nucl. Instrum. Methods Phys. Res., Sect. B* **316**, 210 (2013).
- [11] M. L. Nietiadi and H. M. Urbassek, *Appl. Phys. Lett.* **103**, 113108 (2013).
- [12] M. L. Nietiadi, L. Sandoval, H. M. Urbassek, and W. Möller, *Phys. Rev. B* **90**, 045417 (2014).
- [13] C. Ronning, C. Borschel, S. Geburt, and R. Niepelt, *Mater. Sci. Eng., R* **70**, 30 (2010).
- [14] A. Johannes, S. Noack, W. Paschoal, Jr., S. Kumar, D. Jacobsson, H. Pettersson, L. Samuelson, K. A. Dick, G. Martinez-Criado, M. Burghammer *et al.*, *J. Phys. D* **47**, 394003 (2014).
- [15] A. Johannes, S. Noack, W. Paschoal, Jr., S. Kumar, D. Jacobsson, H. Pettersson, L. Samuelson, K. A. Dick, G. Martinez-Criado, M. Burghammer *et al.*, *J. Phys. D* **48**, 079501 (2015).
- [16] G. Greaves, J. A. Hinks, P. Busby, N. J. Mellors, A. Ilinov, A. Kuronen, K. Nordlund, and S. E. Donnelly, *Phys. Rev. Lett.* **111**, 065504 (2013).
- [17] P. Sigmund, *J. Mater. Sci.* **8**, 1545 (1973).
- [18] S. A. Norris, M. P. Brenner, and M. J. Aziz, *J. Phys.: Condens. Matter* **21**, 224017 (2009).
- [19] S. A. Norris, J. Samela, L. Bukonte, M. Backman, F. Djurabekova, K. Nordlund, C. S. Madi, M. P. Brenner, and M. J. Aziz, *Nat. Commun.* **2**, 276 (2011).
- [20] J. C. Perkinson, E. Anzenberg, M. J. Aziz, and K. F. Ludwig, *Phys. Rev. B* **89**, 115433 (2014).
- [21] M. P. Harrison and R. M. Bradley, *Phys. Rev. B* **89**, 245401 (2014).
- [22] A. Gray, *Modern Differential Geometry of Curves and Surfaces* (CRC Press, Boca Raton, 1993).
- [23] J. P. Biersack and W. Eckstein, *Appl. Phys. A* **34**, 73 (1984).

- [24] J. P. Biersack and L. G. Haggmark, *Nucl. Instrum. Methods* **174**, 257 (1980).
- [25] J. F. Ziegler, SRIM: <http://www.srim.org/>.
- [26] W. Möller, *Nucl. Instrum. Methods Phys. Res., Sect. B* **322**, 23 (2014).
- [27] W. D. Wilson, L. G. Haggmark, and J. P. Biersack, *Phys. Rev. B* **15**, 2458 (1977).
- [28] J. Lindhard and M. Scharff, *Phys. Rev.* **124**, 128 (1961).
- [29] O. S. Oen and M. T. Robinson, *Nucl. Instrum. Methods* **132**, 647 (1976).
- [30] W. D. Luedtke and U. Landman, *Phys. Rev. B* **40**, 1164 (1989).
- [31] F. H. Stillinger and T. A. Weber, *Phys. Rev. B* **31**, 5262 (1985).
- [32] J. F. Ziegler, J. P. Biersack, and U. Littmark, *The Stopping and Range of Ions in Solids* (Pergamon, New York, 1985).
- [33] P. Sigmund, *Appl. Phys. Lett.* **25**, 169 (1974); **27**, 52 (1975).
- [34] H. H. Andersen, *Mat. Fys. Medd. K. Dan. Vidensk. Selsk.* **43**, 127 (1993).
- [35] H. M. Urbassek, in *Ion Beam Science: Solved and Unsolved Problems*, edited by P. Sigmund (Royal Danish Academy of Sciences, Copenhagen, 2006), Vol. 52 of *Mat. Fys. Medd. Dan. Vid. Selsk.*, pp. 433–463.